



# Formation and Reconnection of Electron Scale Current Layers in the Turbulent Outflows of a Primary Reconnection Site

Giovanni Lapenta<sup>1,2</sup> , Martin Goldman<sup>3</sup>, David L. Newman<sup>3</sup> , and Stefan Eriksson<sup>4</sup> <sup>1</sup> Center for Mathematical Plasma Astrophysics, Department of Mathematics, University of Leuven, KU Leuven, Belgium; [giovanni.lapenta@kuleuven.be](mailto:giovanni.lapenta@kuleuven.be)<sup>2</sup> Space Science Institute, Boulder, CO, USA<sup>3</sup> Center for Integrated Plasma Studies, University of Colorado, Boulder, CO, USA<sup>4</sup> Laboratory for Atmospheric and Space Physics, University of Colorado, Boulder, CO, USA

Received 2022 August 11; revised 2022 September 20; accepted 2022 October 7; published 2022 December 6

## Abstract

We simulate with 3D particle in cell, the spontaneous formation of turbulent outflows in an initially laminar 3D reconnecting current layer. We observe the formation of many secondary current layers and reconnection sites in the outflow. The approach we follow is to study each individual feature within the turbulent outflow. To identify all clusters of current in the outflow we use a clustering technique widely used in unsupervised machine learning: density-based spatial clustering of applications with noise. Once the clusters are identified we measure their size and compute reconnection indicators to establish which are undergoing reconnection. With this analysis we establish that the size of the current clusters reaches all the way from its initial system scale down to subelectron skin depth scale. We observe that the smaller current clusters are more prone to reconnecting and to releasing energy. We then find the process of reconnection of the smaller current cluster to be of the recently observed electron-only type that leaves the ions essentially unaffected.

*Unified Astronomy Thesaurus concepts:* [Interplanetary turbulence \(830\)](#); [Solar magnetic reconnection \(1504\)](#)

## 1. Introduction

Reconnection is believed to be central in converting energy from magnetic fields to the kinetic motion of electrons and ions (Biskamp 2000). Astrophysical objects from kiloparsec-scale jets from active galaxies (Sironi & Spitkovsky 2014) to solar atmospheres and planetary magnetospheres (Bhattacharjee 2004) require reconnection to release the magnetic energy into dramatic displays of cosmic proportion. It is often quoted that a solar flare can release in a few seconds the energy of billions of megaton-scale nuclear weapons.

Understanding this energy release has been a grand challenge in the last few decades (Birn & Priest 2007). The great progress made in the last two decades of understanding how reconnection can proceed sufficiently fast has been summarized in textbooks (Biskamp 2000; Birn & Priest 2007) and is a milestone in the progress of space science. The famous Geospace Environmental Modeling (GEM) challenge (Birn et al. 2001) brought understanding on how a single reconnection site can progress on fast (defined as Alfvénic) timescales thanks to the separation of scales of electrons and ions with the formation of different ionic and electronic regions of decoupling from the magnetic field lines. The crowning achievement came when the Magnetospheric Multiscale (MMS) mission encountered one of the predicted electron diffusion regions (Burch et al. 2016), a critical observation necessary to demonstrate that the separation of behavior of electrons and ions is one of the root causes of fast reconnection (Biskamp 2000).

The puzzle now has a major new piece in its place, but the research still needs to find how the pieces fit in transferring fast reconnection from a single site to the global macroscopic

system-scale process of energy transfer. For example in a kiloparsec-size jet we have reconnection electron scales at the tens-of-meters scale (Kronberg et al. 2011), a chasm of 20 orders of magnitude. In the solar corona the electron scale of reconnection is centimeters within reconnecting magnetic arcades of the megameter scale (Vršnak et al. 2009). We need to understand how to bridge this tremendous gap in scales. To explain energy conversion we do not just need fast reconnection, we need fast reconnection to fill a large portion of the system.

To reach the second goal, much attention has gone into considering turbulence. The scenario, outlined in a seminal cartoon in the textbook of Tajima & Shibata (2018), is that of a wide region occupied by a current layer breaking up into a turbulent self-similar multitude of reconnection sites at different scales. Studies of decaying (Matthaeus & Lamkin 1986) or driven (Lazarian & Vishniac 1999) reconnection shows indeed the possibility to obtain large volumes filled with turbulent reconnection. In this case, important new results have looked into initial states that are already turbulent and tracked how reconnection subsequently develops. The turbulent process produces magnetic islands of different sizes with reconnection sites between them on the ion (Servidio et al. 2009) or electron scale (Arrò et al. 2020).

Reconnection can also start laminar but lead itself to a turbulent regime. This is the case of the plasmoid instability leading to the break up of a current layer into multiple islands (Bulanov et al. 1979; Loureiro et al. 2007; Comisso et al. 2016) where reconnection-induced flows feed other reconnection sites and promote a fast process of reconnection (Lapenta 2008; Singh et al. 2019). Recent work has focused on one specific scenario where reconnection leads to a turbulent state: reconnection is initialized at a single reconnection site, where the flow out of that first reconnection site produces a multiplicity of secondary reconnection sites that suggest the possible scenario of a chain reaction of progressively smaller



Original content from this work may be used under the terms of the [Creative Commons Attribution 4.0 licence](#). Any further distribution of this work must maintain attribution to the author(s) and the title of the work, journal citation and DOI.

reconnection sites generated by the turbulent flow (Vapirev et al. 2013; Lapenta et al. 2015).

In the present Paper we investigate this last scenario and consider an initially laminar current layer and follow it as it is disrupted by a perturbation introduced externally. The flow indeed becomes turbulent (Pucci et al. 2017) with the development of secondary reconnection sites (Lapenta et al. 2016b) accompanied by the transformation of magnetic energy into kinetic energy that fills a large portion of the volume (Lapenta et al. 2016a). These regions of secondary reconnection are, in fact, potentially more interesting than the initial primary reconnection site.

The question we intend to address in the present Paper is how can we best characterize these turbulent regions of secondary reconnection? Traditionally turbulence is characterized by statistical correlations: self-similarity is the central discovery of the Kolmogorov scaling, the most sublime outcome of turbulence studies (Frisch & Kolmogorov 1995).

In our system, however, the turbulence of the flow is very spatially dependent (Pucci et al. 2017). In the central reconnection site and in the main inflow region the flow is essentially laminar. In the outflow it becomes more turbulent as one moves deeper into the outflow. Many statistical techniques can be used for this case, correlating space location with local turbulence properties (Pucci et al. 2017, 2018; Arrò et al. 2020; Yang et al. 2022). Intermittence and high spatial variability are characteristic of the system under investigation.

Here we want to try a different approach. We break down turbulence into its individual features. Obviously this approach is daunting for the human mind: one needs to identify and classify all the structures present in the current-carrying regions. The structures vary in size from the macroscopic system scale down to the electron scale at the limit of the resolution of the simulations, which is also at the limit of the range of scales over which a plasma can respond: below, electron scale shielding prevents further breakdown to smaller scales.

If this task is daunting for the human mind, it is the domain of the now pervasive artificial intelligence. We report here on the use of a widely used clustering technique called density-based spatial clustering of applications with noise (DBSCAN; Ester et al. 1996). With this technique, a computer can identify all clusters from large to small and classify all cells within the current-carrying regions into different clusters. With this information we can then break down the turbulent system into individual features and study their properties at different scales by simply measuring quantities in each individual cluster. A readily doable task for a computer, once all the clusters have been identified. In this Paper, we focus on electron currents of any provenance, but the same DBSCAN-based approach can focus on other types of features such as for example, density humps or cavities and magnetic field holes. What we show is one example of a whole category of possible applications of the DBSCAN clustering approach.

Using this analysis we found 209 clusters of localized current within the reconnection outflow ranging in size from the ion to the electron inertial length. We then analyze each individual cluster and ask the following question: is there indication of reconnection in proximity of a given current layer? We answer this question considering three indicators of reconnection: presence of a parallel electric field, presence of agyrotropy, and dissipation in the electron frame. We find that

reconnection is more likely for the smaller layers on the electron scale.

We confirm this finding using a recently proposed indicator that is based on the properties of a class of Lorentz transformations that eliminate the local magnetic field (Lapenta 2021). We find that two populations of current clusters exist: one where agyrotropy, dissipation, and parallel electric field are all large and one where they are small. The Lorentz indicator flags reconnection in the current layers of the first group but not in the second. This tests confirms that the current structures identified as reconnecting are indeed truly reconnecting. Having identified many secondary reconnection sites in the outflow of the primary reconnection site we observe that they are predominantly on the electron scales. A question then becomes obvious: are these processes conventional reconnection with both ions and electrons participating in the process or, given the small size, do these reconnection events belong to the newly observed electron-only type encountered by MMS in its explorations of the dayside of the Earth's magnetosphere as described by Phan et al. (2018)? To address this question we compare the electron and ion contribution to the current and observe that in all reconnecting layers at the electron scale the ion current comprises only a small fraction of the total. We then select four of these electron scale reconnecting sites and make a virtual fly-through that produces a signature comparable to what one would find in a real satellite crossing of one of these structures. We observe for all four of them the signatures of reconnection accompanied by a strong electron jet. The ion flow remains completely unaffected, indicating the regime of electron-only reconnection.

The conclusion then is that turbulence initiated by the interaction of the reconnection outflow from a primary reconnection site inhabits a large portion of the domain and causes a plethora of reconnecting currents at various sizes. The electron scale currents tend to reconnect the most and they reconnect via electron-only reconnection.

The manuscript is organized as follows. Section 2 describes the simulation procedure used to study the evolution of an initially laminar current layer. Section 3 describes the clustering method used to identify all current structures at all sizes based on the clustering technique DBSCAN, widely used in unsupervised machine learning (ML).

Section 4 reports the analysis of the clusters identified by DBSCAN in terms of reconnection and its properties. A summary of the conclusions reached is provided in Section 5.

## 2. Simulation Setup

We consider a 3D fully kinetic simulation of reconnection outflows conducted with the iPic3D particle-in-cell (PIC) code (Markidis & Lapenta 2010). We consider the same type of simulation recently reported in (Lapenta et al. 2015), it uses a modified Harris equilibrium (Harris 1962; Yamada et al. 2000):

$$\mathbf{B}(y) = B_0 \tanh(y/L) \hat{\mathbf{x}} + B_g \hat{\mathbf{z}} \quad (1)$$

$$n(y) = n_0 \operatorname{sech}^2(y/L) + n_b, \quad (2)$$

defined by the thickness  $L/d_i = 0.5$  and with the parameters  $m_i/m_e = 256$ ,  $v_{the}/c = 0.045$ , and  $T_i/T_e = 5$ . We include a mild guide field  $B_g/B_0 = 0.1$  and a background plasma of  $n_b/n_0 = 0.1$ , where  $B_0$  is the asymptotic in-plane field and  $n_0$  is the peak Harris density. All units are normalized and the

results will be given in nondimensional units. The ion inertial length  $d_i$  is defined with the reference Harris density  $n_0$ .

In the coordinates chosen, the initial Harris magnetic field is along  $x$  with size  $L_x = 40d_i$ , the initial gradients are along  $y$  with  $L_y = 15d_i$ . The third dimension, where the initial current and guide field are directed, is initially uniform with  $L_z = 10d_i$ . Open boundaries are imposed in  $x$  and  $y$  and periodicity is assumed along  $z$ . The grid resolution is higher with  $1200 \times 450 \times 300$  cells, resolving the electron skin depth, in the reconnecting background plasma  $\Delta x \approx 0.2d_{e,b}$  (the initial Harris plasma is quickly swept away by reconnection). The time step also well resolves the electron cyclotron frequency, even in the strongest field,  $\omega_{ce,B \max} \Delta t \approx 0.3$  (and even better for more typical fields). Each plasma species is described by two populations of  $5^3$  computational particles per cell; one represents the Harris density ( $n_0 \text{sech}^2(y/L)$ ) and the other the background  $n_b$  nondrifting. The current is initially entirely by the electrons to avoid a relative drift between the two ion species that is known to cause the ion-ion kink instability (Karimabadi et al. 2003). A total of 81 billion particles and 162 million cells are used in a supercomputer parallel topology of  $50 \times 30 \times 20$  (i.e., 30,000) processors.

Reconnection is initialized with a uniform perturbation along  $z$ , very localized in the center of the domain with the exact analytical formulation described in Lapenta et al. (2015). The evolution of the system is described in detail in our previous works (Lapenta et al. 2015, 2016a, 2020b; Pucci et al. 2017): the initial perturbation quickly produces a primary reconnection region that initiates the evolution leading to a strong outflow that interacts with the surrounding plasma forming pileup regions. The outflow develops instabilities driven by the density gradients, the unfavorable curvature of the field lines, by velocity shears and counter streaming beams, and other anisotropic velocity distributions (Vapirev et al. 2013; Sitnov et al. 2014; Divin et al. 2015; Ashour-Abdalla et al. 2016; Pritchett & Runov 2017). The nonlinear evolution leads to turbulence (Price et al. 2017; Pucci et al. 2017; Lapenta et al. 2020a, 2020b) and secondary reconnection sites (Lapenta et al. 2015; Lapenta 2021). The presence of these secondary reconnection sites has been confirmed by analysis of Cluster (Liu et al. 2018) and MMS crossings (Zhou et al. 2021).

We report here the conditions at cycle 18,000, corresponding to  $\omega_{pit} = 1800$  when we stop the simulation as the pileup region is reaching the boundary and is about to exit. Given that  $\omega_{ci}/\omega_{pi} = 0.02165$ , the final time is  $\omega_{cit} = 38.97$ , assuming in these quantities the density  $n_0$  and the magnetic field  $B_0$ .

An example of the simulation results are shown in Figure 1 reporting two different views of the electron current at the cycle 18,000. The outflow from the central reconnection region becomes turbulent, with the turbulence becoming more intense as the distance from the center increases.

The turbulent nature of this outflow has been investigated for very similar simulation setups in previous work (Pucci et al. 2017) where the properties of turbulence were computed in subdomains at different distances from the central reconnection site. The turbulent cascade was followed down to the electron scales and the transition was observed from the Kolmogorov inertial range to dissipation ranges where the power law becomes steeper. Further analysis of the energy exchanges in this simulation at different distances from the central  $x$ -point in the inflow and outflow were reported in Lapenta et al. (2020b). These studies identified the intermittency of the turbulence

observed and correlated the presence of strong currents with the existence of strong energy dissipation (Pucci et al. 2017). The particles are especially strongly energized in the end regions of the outflows where the turbulence becomes strongest (Lapenta et al. 2020b).

These studies had the goal of finding correlations between quantities in an average sense, as it is typical of turbulence studies. What the previous studies did not investigate is the detailed individual features observed within the outflows. What precisely are the individual current layers, where are they located, and what size do each one of them have? This is counter to the usual view of trying to extract global properties of turbulence without looking at the specific detail of each substructure. Finding each specific feature and characterizing it seems like an impossible task. For the human mind it is impossible and exceedingly boring. But not for an artificial intelligence.

### 3. Method of Clustering Analysis

True turbulence is a process that relies on commonalities of processes at different scales. Concepts like scale invariance and self-similarity can describe these aspects. Traditionally statistical correlations, Fourier analysis, or structure functions of different orders are used to capture this nature of turbulence.

However, the outflow of a reconnection site presents the transition of a flow from laminar in the close proximity of the electron diffusion region (EDR) to progressively more chaotic and turbulent in the farther parts of the jet. Studies of correlations and structure function have shown the development of Kolmogorov scaling at large scales with other power-law indices at ion and electron dissipation scales (Pucci et al. 2017).

What we intend to do here is different, we do not want to assume turbulence is fully developed and we want to collect individual information about all features at all scales presented by the electron current. In a sense this is going back to the level of stamp collecting. We want to collect all the current layers formed from the smallest to the largest and identify the properties of each one of them and see if in this spatial information we can capture some deeper physical meaning.

In 3D large-scale simulations, like the present one, identifying each current layer by eye is a daunting job. But now it is a job artificial intelligence can do readily. We use a specific very widely used algorithm to identify each individual current layer: density-based spatial clustering of applications with noise (DBSCAN; Ester et al. 1996).

DBSCAN is a density-based algorithm that collects data points in a given space, aggregates points that are tightly grouped together, forming aggregates of near neighbors. Outliers in low density regions are not spuriously aggregated with others. DBSCAN is automatic and relatively undemanding from a computational perspective. DBSCAN is based on a distance function: we use the Cartesian norm, a neighborhood radius  $\epsilon$  that we set to five grid points, and a minimum number of points to distinguish a cluster from isolated outliers that we also set to five. Five might seem like an arbitrary anthropomorphic choice. However testing this choice proves the results are insensitive to it. We note that five is also the distance over which iPic3D smooths the interpolation functions so it is justified to assume that points beyond a distance of five grid cells are not direct neighbors as seen by the PIC algorithm. On the other hand groups of cells of fewer than five points are

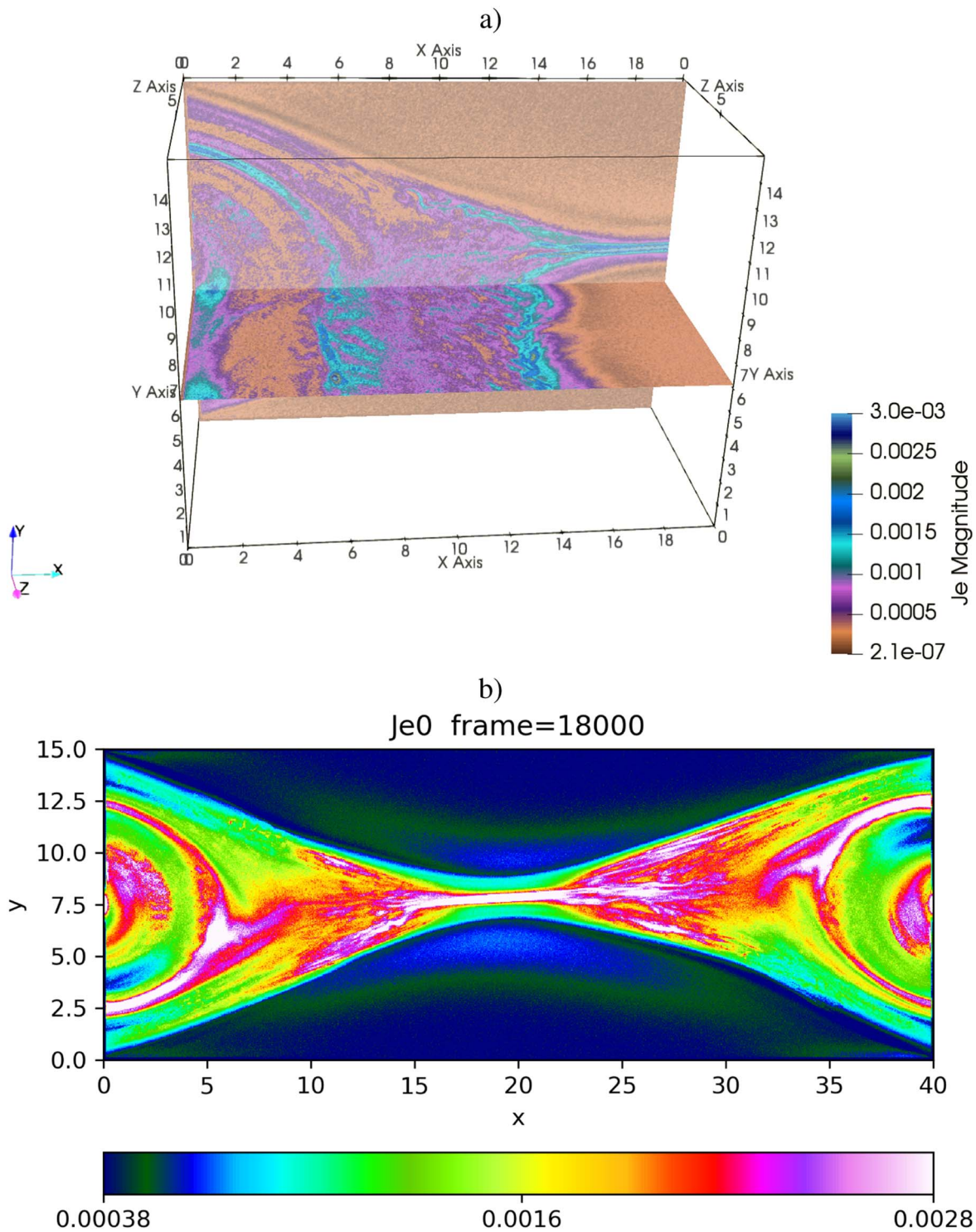


**Figure 1.** Magnitude of the electron current. Panel (a) shows a 3D visualization with two different cuts with a color scale that highlights the local turbulent variations of the current. Panel (b) is a 2D cut at  $z = L_z/2$  using a different color scale.

suspiciously close to numerical noise given the choice of five cells for the smoothing functions.

DBSCAN has already been used successfully for a similar task of identifying currents where potential reconnection regions are in 2D simulations (Sisti et al. 2021) and for clustering large numbers of particles in petascale 3D simulations (Patwary et al. 2015). Moreover, DBSCAN is an algorithm widely used in countless machine-learning applications and is a core algorithm of most ML toolkits like the

MATLAB ML toolkit or Sci-Kit in python. We use here the same approach implemented in the MATLAB ML toolkit to cluster the current layers observed in the simulation at a given time.

The first step is to define what a current layer is. This has a component of arbitrariness because the electron current almost never vanishes completely. Figure 1 shows a cut of the magnitude of the electron current  $J_e$ . We need a threshold above which we consider a current intense enough to be

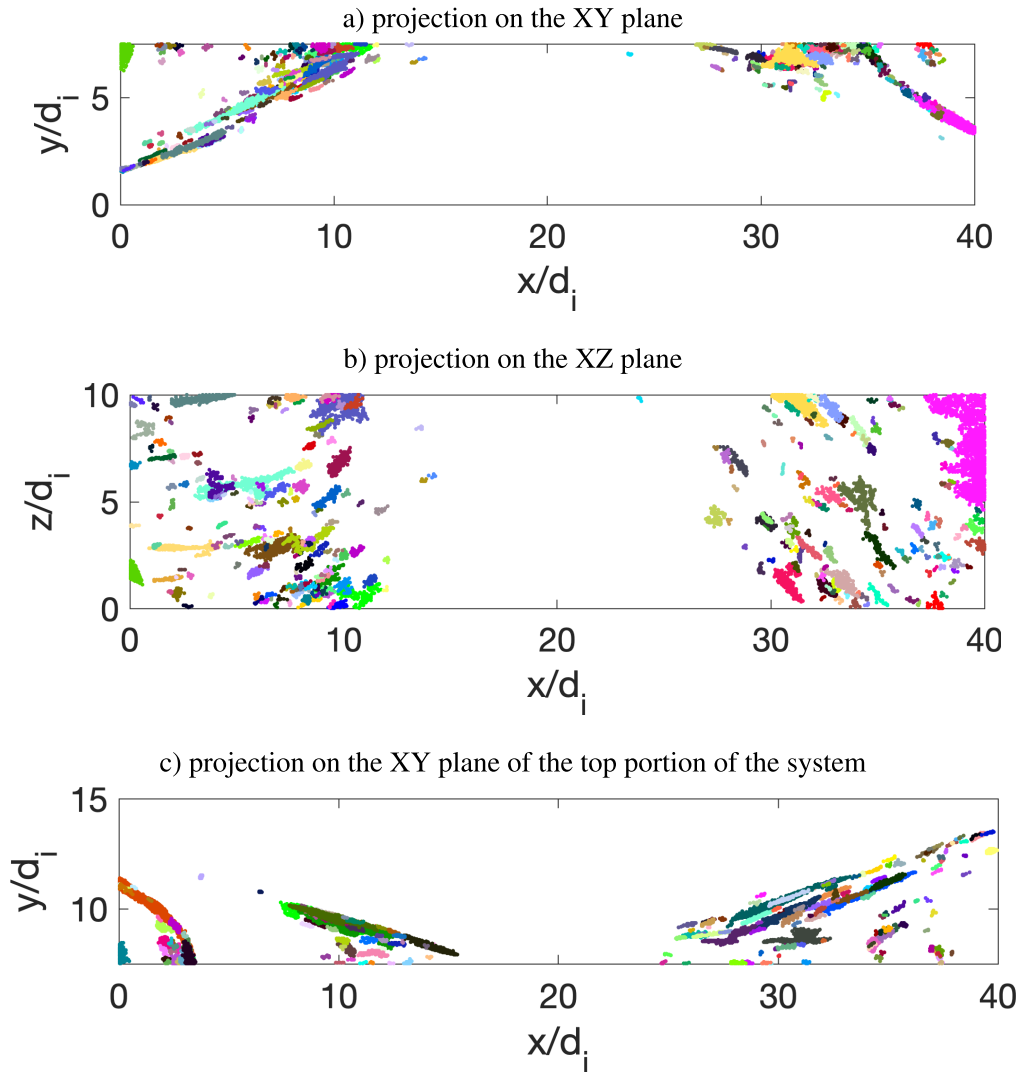


**Figure 2.** Orthogonal views of the current layers identified by the DBSCAN clustering algorithm for the bottom (panels (a) and (b)) and top (panel (c)) of the system. Each cluster is shown with a different color. The big central laminar current sheet at  $x = L_x/2$  is not shown to avoid overcrowding the figure. Each pixel shown is one cell of the computational domain flagged as carrying a significant electron current.

considered for clustering. If we use too low a value all points will be considered current carrying and if we set too high a value we miss important current regions. After considering different options often used in the literature, we flagged as binary 1, all pixels in our 3D uniform grid where the square of the electron current exceeded one-tenth of the maximum value. DBSCAN then clustered all pixels with binary value 1 to obtain all clusters of currents identified by this procedure.

Alternative procedures to identify the cells of the computational grid where we consider the electron current to be significant lead to results that are different in details but do not alter the conclusions of the analysis with DBSCAN that we report below.

#### 4. Identification of the Current Sheets and Their Properties

With the use of data mining and artificial intelligence, we no longer look for statistical correlations but we identify every current layer, as a cluster of current-carrying pixels (a 3D pixel is a cell in the computational grid) and measure its properties. First we can count the number of currents identified and show them using different colors for each cluster. Figure 2 shows two

views of the 3D clustering provided by DBSCAN. The area considered is only half of the system ( $y < L_y/2$ ) by virtue of the cross symmetry of reconnection in the presence of guide fields (left-top symmetric with right-bottom and vice-versa). Figure 2 reports for comparison also the top part for reference.

The DBSCAN algorithm finds 290 current layers (including the big central laminar one that is not included in the representations shown in Figure 2). On a single processor laptop the procedure takes hours of CPU time and it is most conveniently run overnight. We relied on a simple Matlab implementation on CPUs but DBSCAN can be applied more efficiently on accelerator processors with much better performances (Ji & Wang 2021).

From preliminary inspection it is clear that some current structures are on the ion scale but some others are made of few pixels and are on the electron scales. Note that DBSCAN excludes as outliers isolated pixels that could in fact be tiny current layers on the electron scale, but could also be noise. The DBSCAN setup used excludes the smallest clusters of fewer than five cells.

Having now identified all 290 of the current layers we can study the properties of each one of them and their individual

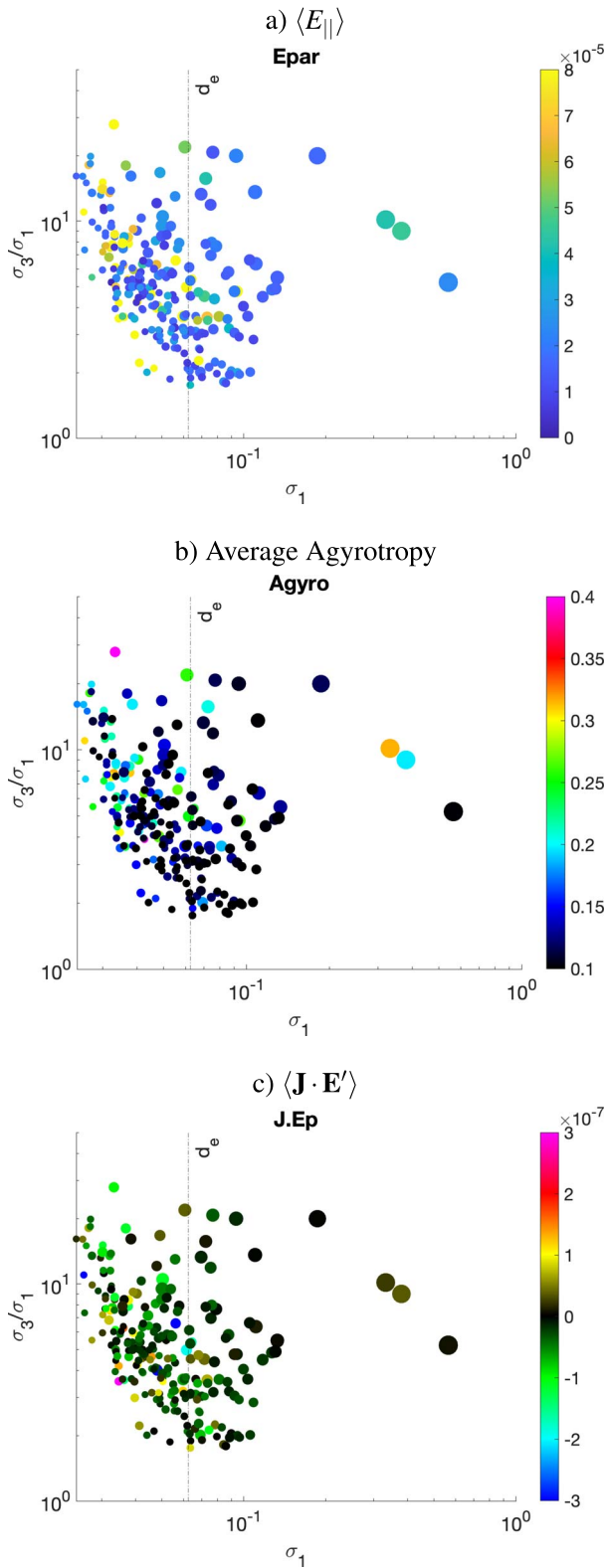


**Figure 3.** Scatter plot of the identified current layers. Each layer is characterized with an ellipsoid with three axes:  $\sigma_1$ ,  $\sigma_2$ ,  $\sigma_3$ , ordered in decreasing size. The plot shows the major axis (length of the current layer) on the abscissa and the aspect ratio of the smallest to the largest axis of each current cluster (modeled as an ellipsoid) in the ordinate. From top to bottom: (a) parallel electric field, (b) agyrotropy, (c) dissipation in the electron comoving frame, all averaged over the cells comprising the current layer.

relation with other quantities. Dealing with 290 clusters is a lot easier than dealing with  $1200 \times 450/2 \times 300$  (i.e., 81 million)

individual cells. The DBSCAN procedure has reduced dramatically the number of the individual entities we need to analyze. While not the most engaging activity imaginable, one can flip through 290 things and observe them one by one. But we will not do that and let, instead, automatic analysis run over these 290 clusters.

#### 4.1. Signatures of Reconnection

We consider the first three indicators of reconnection to see what is the correlation between the current size and its likelihood to be reconnecting. Figure 3 reports a scatter plot of all identified currents. Each current layer is measured for its primary size defined by fitting each layer with an ellipsoid. To do this we used the Gaussian fit that identified the three primary orthogonal axes of each current structure:  $\sigma_1$ ,  $\sigma_2$ ,  $\sigma_3$  in decreasing order. Each current is represented with a dot sorted by its main size (current length) and aspect ratio (between minimum and maximum axis of the ellipsoid). Each dot is then sized proportionally to the number of cells it encompasses and it is colored based on three often used indicators of reconnection: parallel electric field,  $E_{||}$  (panel (a)), electron agyrotropy (panel (b); Scudder et al. 2008), and dissipation in the electron frame,  $\mathbf{J} \cdot \mathbf{E}'$  where  $\mathbf{E}'$  is the electric field in the electron frame,  $\mathbf{E} + \mathbf{v}_e \times \mathbf{B}$  (panel (c); Zenitani et al. 2011). These indicators are averages over all the cells identified by DBSCAN as being part of one current layer. As can be observed, the parallel electric field and agyrotropy are large primarily at small scales, at the electron skin depth scale, or less. We have excluded in this representation the big primary reconnection current layer in the center of the domain because it is of course reconnecting and well known. We focus instead on the smaller current formations in the outflow. As can be seen in panel (a), the parallel electric field has its highest values (in yellow) for the smallest current layers with  $\sigma_1$  being the smallest. Agyrotropy also is smallest for the same range of  $\sigma_1$ . The dissipation measure,  $\mathbf{J} \cdot \mathbf{E}'$ , concurs obtaining the largest (positive and negative) values in the same range.

This analysis then suggests that the smallest layers on the electron skin depth and smaller are the most active, producing the most intense signature of reconnection and with the most intense energy conversion.

#### 4.2. Lorentz Reconnection Indicator

Recently, an alternative way has been proposed for detecting regions of reconnection (Lapenta 2021). In the vicinity of a reconnection point, the speed of the local Lorentz transformation that eliminates the in-plane magnetic field is of course zero because reconnection by definition eliminates the in-plane component of the magnetic field. However, everywhere else the speed of this transformation is very high. When the constraint is added to make a Lorentz transformation that maintains its alignment with the local electric field (Lapenta 2021), this speed can exceed even the speed of light, making the transformation impossible. A simple method for detecting reconnection regions is then that of computing the speed of the local Lorentz transformation aligned with the laboratory electric field that eliminates the component of the magnetic field normal to the electric field:

$$\frac{v_L}{c} = c \frac{\mathbf{E} \times \mathbf{B}}{E^2}. \quad (3)$$

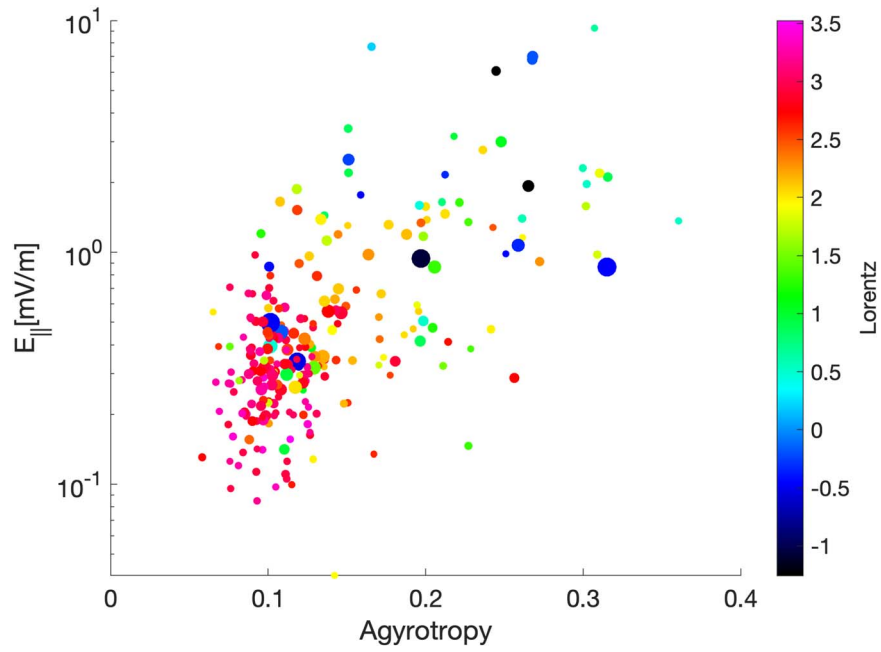


**Figure 4.** Scatter plot of the identified current layers based on their average agyrotropy and average parallel electric field. The dot size is proportional to the number of cells forming the current and their color is proportional to the measured Lorentz reconnection indicator, in logarithmic scale,  $\log_{10}(v_L/c)$  (Lapenta 2021).

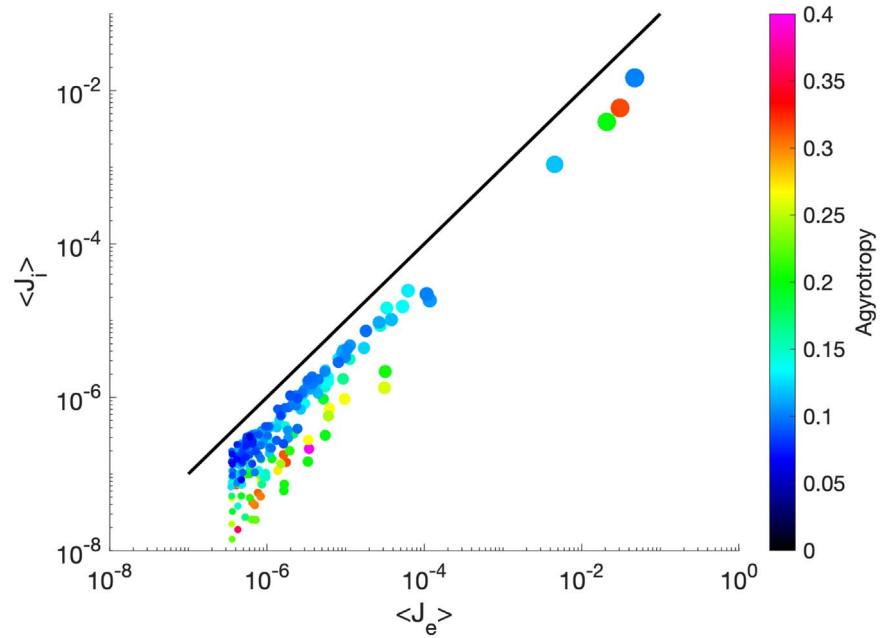


**Figure 5.** Scatter plot of the identified current layers based on their average ion and electron current. The size of each dot is proportional to the volume of the current layer and their color represents the average agyrotropy as shown in the colorbar.

When this speed becomes small, we are in the proximity of a reconnection site, either an  $x$ -point, or a  $o$ -point in 2D, or one in a class of six different types of points in 3D (Lapenta 2021). We have tested this indicator and compared it with the other more traditional indicators listed above. To do so, acknowledging that reconnection is not happening at the current sheet per se but it might be in its vicinity, we have added five cells of padding in each direction around each identified current cluster for detecting the smallest value of the Lorentz indicator. We also tried to change the padding to fewer or more cells and the conclusions were not affected.

Figure 4 shows all identified current layers according to their average agyrotropy and magnitude of the parallel electric field. The dots are colored according to the Lorentz indicator. As can be seen, the distribution of point is bimodal. At low agyrotropy and low parallel electric field (lower-left part), the Lorentz indicator shows a very high speed for the transformation, in fact many orders of magnitude above the speed of light. There is no reconnection flagged in this case. At high agyrotropy and high parallel electric field (upper-right part) the current layers show a small velocity for the Lorentz indicator flagging reconnection. The Lorentz transformation indicator then concurs with the other measures of reconnection; a further

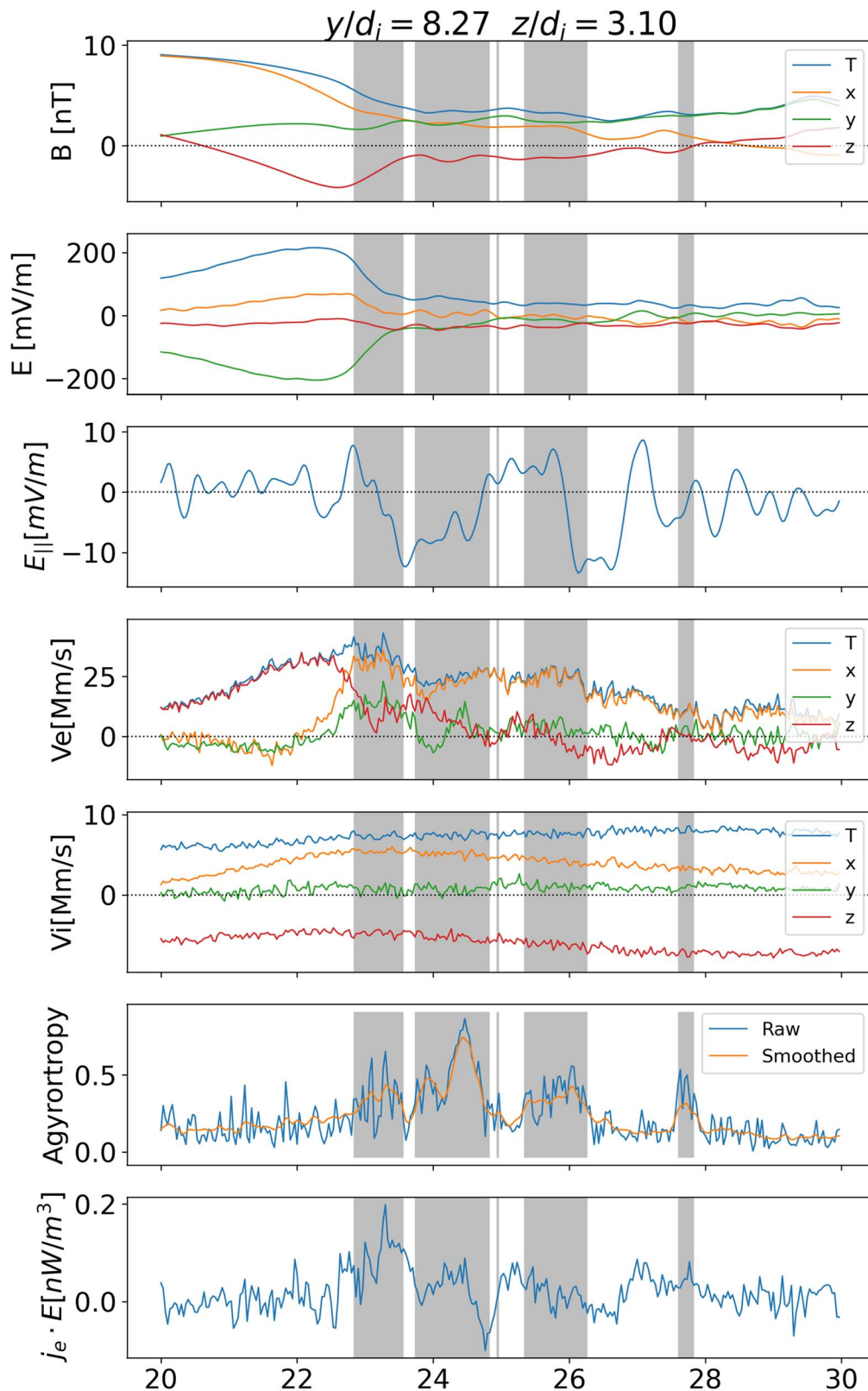


**Figure 6.** Virtual probe sweeping through the domain along  $x$  at  $y = 8.27$  and  $z = 3.1$ . From top to bottom reported are: magnetic field  $B/B_0$ , electric field  $eE/m_i c \omega_{pi}$ , parallel electric field  $eE_{\parallel}/m_i c \omega_{pi}$ , electron speed  $V_e$ , ion speed  $V_i$ , agyrortropy, electron and ion density ( $n/4\pi n_0$ ), and dissipation  $\mathbf{J} \cdot \mathbf{E}$ . To facilitate comparison with observational data we have betrayed a theoretician’s best instinct and used physical units instead of normalized dimensionless units.

confirmation of the conclusions reported above and a confirmation of the usefulness of the Lorentz reconnection indicator.

#### 4.3. Is Reconnection Electron Only?

We have noted above that most current layers flagged concurrently for reconnection by the parallel electric field,

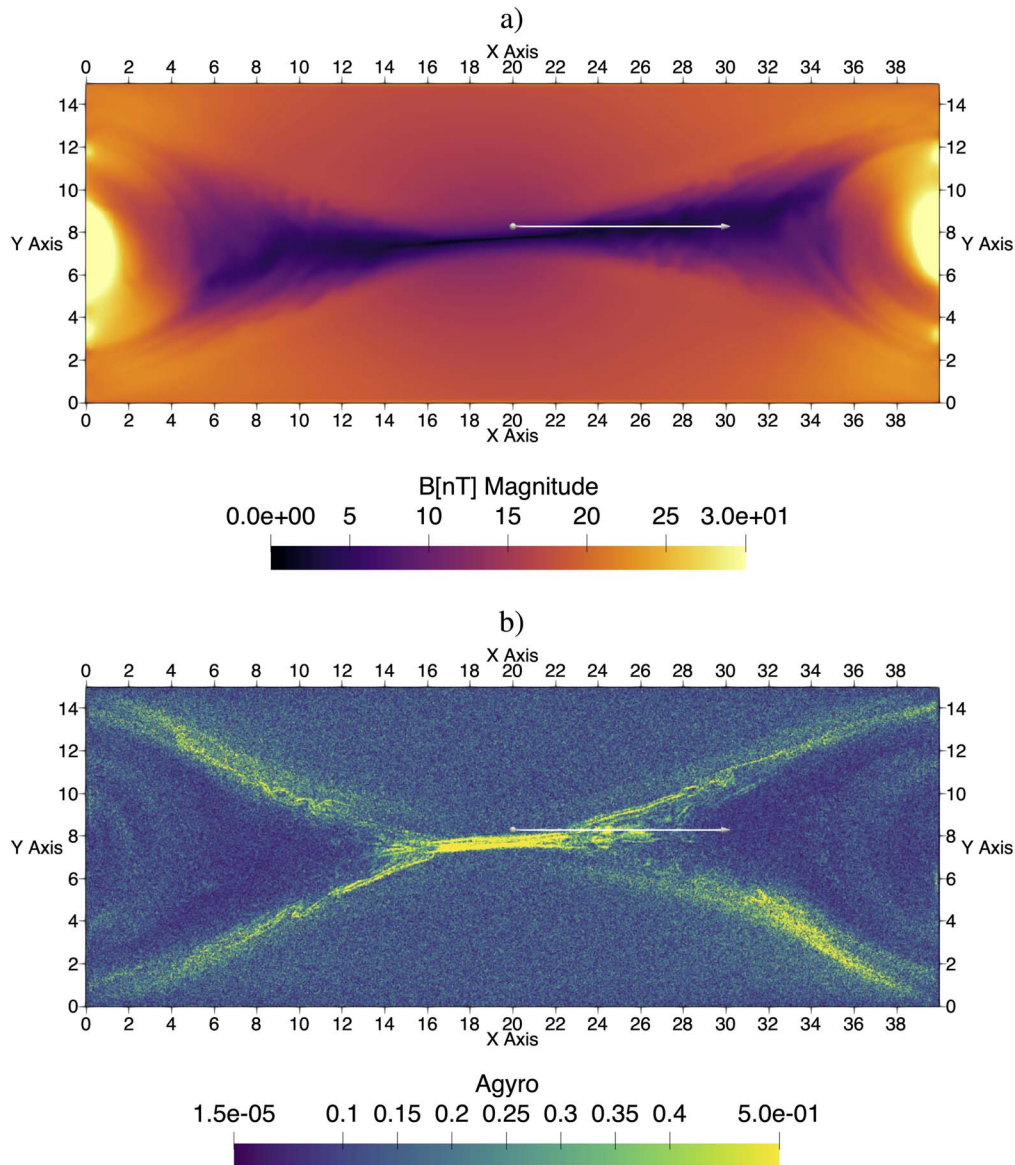


**Figure 7.** Cross section of the domain at the same time used in the previous analysis (cycle 18,000) at  $y = 8.27$ . The path of the virtual probe used in Figure 6 is shown as a white arrow. False color representation of the magnetic field intensity in nT (panel (a)) and of agyrotropy (panel (b)).

agyrotropy, the dissipation in the electron frame, and by the Lorentz reconnection indicator tend to be at small electron scales. The question then is whether these small current layers are in fact exhibiting electron-only reconnection. Identified recently in MMS data (Phan et al. 2018; Stawarz et al. 2019) and observed in dedicated simulations (Sharma Pyakurel et al. 2019; Arrò et al. 2020; Califano et al. 2020; Vega et al. 2020), electron-only reconnection is a regime where reconnection affects only the electrons while the ions show little motion in the vicinity of a reconnection site. This is the type of limit previously studied by electron MHD models that assumed unresponsive ions.

To clarify this point, we consider all current layers and plot them according to their ion and electron current. Given the quasi-neutrality, we expect the normal regime reconnection to have the current carrying in more equal weight by electrons and ions, while in the electron-only regime of reconnection the current should be carried almost entirely by the ions. Figure 5 shows a scatter plot of this representation where each dot is

colored according to the average agyrotropy as a reliable indicator of ongoing reconnection. The size of the dots is again proportional to the size of the current layer measured by the number of cells that belong to it. As can be seen all reconnecting layers have a much larger electron current than ion current and are the smallest current-carrying regions (as measured by the dot size). The combined presence of small current sizes and a large electron current compared with ion current indices indicates that these are possible sites of electron-only reconnection (Chacon et al. 2007).

Obviously this is not a conclusive statement because even in regular reconnection, within the electron diffusion region the electron current dominates. Then it is equally possible we identified electron-only reconnection sites or electron diffusion regions within regular reconnection. The distinction is not clear and in the view of the authors there is no absolutely firm statement to distinguish the two. Only the context can tell. Figure 6 and Figure 7 provide the context for a few selected secondary reconnection sites. A fly-through is shown for a

virtual spacecraft flying across the simulation domain. The path is along the  $x$ -axis but its  $y$  and  $z$  locations are chosen to be encountering some of the small electron scale current layers identified by DBSCAN.

Over the flight path of the virtual spacecraft, we identify in the right-going outflow from the central primary reconnection site, four secondary reconnecting regions, identified by a strong peak in agyrotropy accompanied by peaks (negative or positive) in parallel electric field, and electron current dissipation. The four secondary sites are highlighted by a thin vertical line. Each secondary reconnection site has a peak in the electron speed but the ion flow speed remains completely unaffected. A clear indication of electron-only reconnection.

## 5. Summary and Conclusions

We analyze a turbulent outflow from a primary reconnection site using particle-in-cell simulations. The resolution is refined enough to resolve subelectron scale current layers formed in the turbulent outflow.

We use a well-known clustering method called DBSCAN to identify each current formation from the biggest to the smallest. We identify 290 of them that can be plotted using a color scale that identifies each cluster, allowing visual inspection.

The result of the clustering method is then further analyzed using a 3D Gaussian fit of each cluster, represented as an ellipsoid with three principal axes, with the longest being the length and the other two giving the thicknesses in the other two directions. With this information we can sort the clusters in terms of length, aspect ratio, and volume (simply the number of computational cells forming the cluster).

With this information we can then correlate the size of the current layers with the process of reconnection. We consider three different often used indicators of reconnection (parallel electric field, agyrotropy, and dissipation in the electron frame). All three identify a clear correlation between the size of the current layer and reconnection: the smaller currents reconnect more. We then compared this conclusion with the result of applying a recently proposed indicator based on the Lorentz transformation that eliminates the local magnetic field. The Lorentz indicator concurs with the others confirming its validity and reinforcing the previous conclusions with the other indicators.

Finally we address the question of whether the smallest current layers are reconnecting via conventional reconnection or the electron-only reconnection where the ions remain largely unaffected. We observe that indeed the reconnecting currents are primarily electron currents with little ion motion.

We confirm this conclusion by directly observing four of these small clusters of current and observe that the ions are not visibly affected by the process. The conclusion is then that at the smallest scales not only reconnection is more likely but it is also more likely to be electron-only reconnection.

The relevance of these results is twofold. First, we investigate the properties of turbulent outflows finding many secondary reconnection sites characterized by intense energy dissipation, strong agyrotropy, and large parallel electric fields. Second, we find that in these outflows secondary reconnection tends to be on small electron scale and tends to be of the electron-only type, leaving the ions unaffected.

This project has received funding from the KULeuven Bijzonder Onderzoeksfonds (BOF) under the C1 project

KULeuven Bijzonder Onderzoeksfonds (BOF), from the European Union's Horizon 2020 research and innovation program under grant agreement No. 955606 (DEEP-SEA) and from the NASA grant 80NSSC19K0841. Computing has been provided by NASA at the NAS and NCCS high performance computing facilities, by the Flemish Supercomputing Center (VSC) and by the PRACE Tier-0 program under the AIDA-Space grant. This research used resources of the National Energy Research Scientific Computing Center, which is supported by the Office of Science of the US Department of Energy under Contract No. DE-AC02-05CH11231.

## ORCID iDs

Giovanni Lapenta  <https://orcid.org/0000-0002-3123-4024>  
David L. Newman  <https://orcid.org/0000-0003-0810-1204>  
Stefan Eriksson  <https://orcid.org/0000-0002-5619-1577>

## References

- Arrò, G., Califano, F., & Lapenta, G. 2020, *A&A*, **642**, A45  
Ashour-Abdalla, M., Lapenta, G., Walker, R., et al. 2016, *GeoRL*, **43**, 6005  
Bhattacharjee, A. 2004, *ARA&A*, **42**, 365  
Birn, J., Drake, J. F., Shay, M. A., et al. 2001, *JGR*, **106**, 3715  
Birn, J., & Priest, E. R. 2007, *Reconnection of magnetic fields: magnetohydrodynamics and collisionless theory and observations* (Cambridge: Cambridge Univ. Press)  
Biskamp, D. 2000, *Magnetic Reconnection in Plasmas* (Cambridge: Cambridge Univ. Press)  
Bulanov, S., Sakai, J., & Syrovatskii, S. 1979, *FizPl*, **5**, 280  
Burch, J., Torbert, R., Phan, T., et al. 2016, *Sci*, **352**, aaf2939  
Califano, F., Cerri, S. S., Faganello, M., et al. 2020, *FrP*, **8**, 317  
Chacon, L., Simakov, A. N., & Zocco, A. 2007, *PhRvL*, **99**, 235001  
Comisso, L., Lingam, M., Huang, Y.-M., & Bhattacharjee, A. 2016, *PhPI*, **23**, 100702  
Divin, A., Khotyaintsev, Y., Vaivads, A., et al. 2015, *JGRA*, **120**, 2675  
Ester, M., Kriegel, H.-P., Sander, J., & Xu, X. 1996, in *Proc. Second Int. Conf. Knowledge Discovery and Data Mining* (Washington, DC: AAAI Press), 226  
Frisch, U., & Kolmogorov, A. N. 1995, *Turbulence: the legacy of AN Kolmogorov* (Cambridge: Cambridge Univ. Press)  
Harris, E. G. 1962, *Il Nuovo Cimento (1955-1965)*, **23**, 115  
Ji, Z., & Wang, C.-L. 2021, in *50th Int. Conf. Parallel Processing (ICPP 2021)* (New York: ACM), 1  
Karimabadi, H., Daughton, W., Pritchett, P., & Krauss-Varban, D. 2003, *JGRA*, **108**, 1400  
Kronberg, P. P., Lovelace, R. V. E., Lapenta, G., & Colgate, S. A. 2011, *ApJL*, **741**, L15  
Lapenta, G. 2008, *PhRvL*, **100**, 235001  
Lapenta, G. 2021, *ApJ*, **911**, 147  
Lapenta, G., El Alaoui, M., Berchem, J., & Walker, R. 2020a, *JGRA*, **125**, e27276  
Lapenta, G., Goldman, M. V., Newman, D. L., & Markidis, S. 2016a, *PPCF*, **59**, 014019  
Lapenta, G., Markidis, S., Goldman, M. V., & Newman, D. L. 2015, *NatPh*, **11**, 690  
Lapenta, G., Pucci, F., Goldman, M., & Newman, D. 2020b, *ApJ*, **888**, 104  
Lapenta, G., Wang, R., & Cazzola, E. 2016b, in *Magnetic Reconnection: Concepts and Applications*, ed. W. D. Gonzalez & E. N. Parker (Berlin: Springer)  
Lazarian, A., & Vishniac, E. T. 1999, *ApJ*, **517**, 700  
Liu, C. M., Fu, H. S., Cao, D., Xu, Y., & Divin, A. 2018, *ApJ*, **860**, 128  
Loureiro, N. F., Schekochihin, A. A., & Cowley, S. C. 2007, *PhPI*, **14**, 100703  
Markidis, S., Lapenta, G., & Rizwan-uddin 2010, *Math. Comput. Simul.*, **80**, 1509  
Matthaeus, W. H., & Lamkin, S. L. 1986, *PhFI*, **29**, 2513  
Patwary, M. M. A., Byna, S., Satish, N. R., et al. 2015, in *SC'15 Proc. Int. Conf. High Performance Computing, Networking, Storage and Analysis*, IEEE (Piscataway, NJ: IEEE), 1  
Phan, T. D., Eastwood, J. P., Shay, M. A., et al. 2018, *Natur*, **557**, 202  
Price, L., Swisdak, M., Drake, J., et al. 2017, *JGRA*, **122**, 11086  
Pritchett, P. L., & Runov, A. 2017, *JGRA*, **122**, 3183  
Pucci, F., Matthaeus, W. H., Chasapis, A., et al. 2018, *ApJ*, **867**, 10

- Pucci, F., Servidio, S., Sorriso-Valvo, L., et al. 2017, *ApJ*, **841**, 60
- Scudder, J. D., Holdaway, R. D., Glassberg, R., & Rodriguez, S. L. 2008, *JGRA*, **113**, A10208
- Servidio, S., Matthaeus, W. H., Shay, M. A., Cassak, P. A., & Dmitruk, P. 2009, *PhRvL*, **102**, 115003
- Sharma Pyakurel, P., Shay, M. A., Phan, T. D., et al. 2019, *PhPI*, **26**, 082307
- Singh, K. A. P., Pucci, F., Tenerani, A., et al. 2019, *ApJ*, **881**, 52
- Sironi, L., & Spitkovsky, A. 2014, *ApJL*, **783**, L21
- Sisti, M., Finelli, F., Pedrazzi, G., et al. 2021, *ApJ*, **908**, 107
- Sitnov, M. I., Merkin, V. G., Swisdak, M., et al. 2014, *JGRA*, **119**, 7151
- Stawarz, J. E., Eastwood, J. P., Phan, T. D., et al. 2019, *ApJL*, **877**, L37
- Tajima, T., & Shibata, K. 2018, *Plasma Astrophysics* (Boca Raton, FL: CRC Press)
- Vapirev, A. E., Lapenta, G., Divin, A., et al. 2013, *JGRA*, **118**, 1435
- Vega, C., Roytershteyn, V., Delzanno, G. L., & Boldyrev, S. 2020, *ApJL*, **893**, L10
- Vršnak, B., Poletto, G., Vujić, E., et al. 2009, *A&A*, **499**, 905
- Yamada, M., Ji, H., Hsu, S., et al. 2000, *PhPI*, **7**, 1781
- Yang, Y., Matthaeus, W. H., Roy, S., et al. 2022, *ApJ*, **929**, 142
- Zenitani, S., Hesse, M., Klimas, A., & Kuznetsova, M. 2011, *PhRvL*, **106**, 195003
- Zhou, M., Man, H., Deng, X., et al. 2021, *GeoRL*, **48**, e2020GL091215